separations

MDPI

Article

Highly Acidic Macro-Porous Cation Exchange Resin D001 for Efficient Separation of Co(II) from Nd(III) and Dy(III) During Rare Earth Recycling

Yao Li [1], Huilin An [1], Zezuo Jiang [2,3], Haixiang Tan [2,3] and Chunlin He [1,3,*]

[1] Guangxi Key Laboratory of Processing for Non-Ferrous Metals and Featured Materials, School of Resources, Environment and Materials, Guangxi University, Nanning 530004, China; liyao_ly1999@163.com (Y.L.); 16680924011@163.com (H.A.)
[2] Guangxi Key Laboratory of Advanced Rare Earth Materials, Nanning 530004, China; jiangzezuott@163.com (Z.J.); wjj_thx@163.com (H.T.)
[3] Guangxi Guosheng Rare Earth New Materials Co., Ltd., Chongzuo 532200, China
* Correspondence: helink@gxu.edu.cn; Tel.: +86-15177793711

Abstract

Addressing the need for efficient separation of critical elements from NdFeB magnets, this study introduces, for the first time, a D001 cation exchange resin for the selective separation Co(II) from Nd(III) and Dy(III). At pH 5, the resin adsorbs Nd and Dy with high capacities (97.57 and 86.38 mg/g, respectively) and efficiencies (over 98%), but shows low affinity for Co (26.6% efficiency). The resin exhibits excellent stability across a wide pH range of 2–7 and maintains high adsorption performance over five consecutive cycles. The process follows pseudo-second-order kinetics and the Langmuir model. Co(II) is effectively desorbed with high purity (>99%) using 2.5 M H_2SO_4. Characterization confirms that adsorption occurs via ion exchange on $–SO_3Na$ groups. This method successfully separates Co, providing a high-purity stream for further rare earth purification and demonstrating strong industrial potential.

Keywords: NdFeB; Co-Nd-Dy; adsorption; separation; D001 resin

1. Introduction

The rapid expansion of the new energy, high-end manufacturing, and electronics industries has established neodymium–iron–boron (NdFeB) magnets as a critical material for motors [1], wind turbines [2], and consumer electronics [3], owing to their exceptional magnetic properties. This has led to a continuously growing market demand. The performance of these magnets largely depends on three key elements: dysprosium (Dy), neodymium (Nd), and cobalt (Co). Dysprosium significantly enhances high-temperature stability [4], neodymium serves as the primary constituent [5], and cobalt improves corrosion resistance and mechanical strength [6].

Rare earth elements (REEs) are considered strategically vital due to their widespread use in scientific, technological, military, and industrial applications [7]. In particular, future demand for neodymium and dysprosium is expected to exceed current supply levels [8]. Both REEs and cobalt have been classified as critical raw materials by the European Commission in 2023, reflecting their economic importance and associated supply risks [9]. Therefore, developing efficient, low-consumption, and high-purity separation technologies is essential to support sustainable industrial development and promote resource recycling.

Check for updates

Academic Editor: Guoquan Zhang

Received: 2 February 2026
Revised: 18 February 2026
Accepted: 24 February 2026
Published: 27 February 2026

Copyright: © 2026 by the authors. Licensee MDPI, Basel, Switzerland. This article is an open access article distributed under the terms and conditions of the Creative Commons Attribution (CC BY) license.

The current research landscape reports various technologies capable of recovering valuable metals from NdFeB magnets, predominantly based on hydrometallurgy, including acid leaching [10], solvent extraction [11], ion exchange [12], and adsorption methods [13]. Acid leaching consumes significant amounts of acid and imposes a heavy environmental burden [14]. Solvent extraction employs organic solvents and additives that are often flammable and toxic [15], while organic extractants frequently exhibit emulsification during the extraction process, leading to the formation of a third phase [16]. Conventional ion exchange methods commonly suffer from insufficient selectivity and limited dynamic adsorption capacity within complex, multi-ion competitive systems [17]. Adsorption methods show potential for REE recovery due to their simple process flow, operational convenience, and environmental friendliness. For instance, Nogueira M. [18] et al. converted waste tire rubber into porous carbon adsorbents using pyrolysis and CO_2 activation technology, addressing the need for sustainable adsorbent materials for REE recovery and achieving efficient adsorption of Nd(III) and Dy(III). However, the saturated adsorption capacities were merely 24.7 mg/g and 34.4 mg/g, respectively. In another study, Zhong Y. [19] et al. prepared an N-dodecyl phosphoric acid/calcium alginate (DPPA/CaALG) hybrid hydrogel adsorbent via a sol-gel method, achieving efficient and highly selective separation and recovery of Nd(III) and Dy(III) from highly acidic simulated leachates, with adsorption capacities as high as 162.5 mg/g and 183.5 mg/g, respectively. Nonetheless, the adsorption efficiency of this hydrogel adsorbent dropped to approximately 50% by the third adsorption cycle. These examples highlight the persistent challenges in adsorption methods, such as insufficient selectivity, limited adsorption capacity, and poor cycling stability. Therefore, developing multifunctional adsorbents that are operationally simple, environmentally sustainable, highly selective, and capable of stable long-term performance represents a critical step toward achieving the separation of Co(II) from Nd(III) and Dy(III).

Cation exchange resins have emerged as a significant material for metal separation in complex solutions due to their tunable ion selectivity, stable chemical properties, and well-established industrial application base [20–23]. These resins achieve adsorption through electrostatic interactions between their functional groups and metal ions, and their selectivity can be optimized by coordinated adjustments of resin structure, functional group types, and solution conditions [24,25]. Kovalenko [26] et al. developed a TODGA-impregnated resin (SIR 3) for the recovery of Pr, Nd, and Dy from NdFeB magnet leachates. Although classified as a solvent-impregnated resin, its separation mechanism is based on ion exchange between rare earth ions and the TODGA extractant immobilized on the polymer support. The resin exhibited an adsorption capacity of 128.2 mg/g for Nd and achieved >99.5% purity for individual rare earth elements after chromatographic separation. However, the preparation of this resin requires the synthesis of TODGA and a multi-step impregnation process, which limits its commercial availability and scalability. Moreover, its reusability was only demonstrated over three cycles, which may be insufficient for long-term industrial applications requiring stable cycling performance. The D001-type strong-acid cation exchange resin, with its sulfonic acid functional groups ($–SO_3^-$) [27], exhibits strong affinity for high-valence cations, along with advantages such as excellent chemical stability and high renewability. This provides a reliable material foundation for the efficient enrichment of Nd(III) and Dy(III) from Co(II)-bearing backgrounds.

This study employed a D001 cation exchange resin (sodium form) to achieve the effective separation of Co(II) from Nd(III) and Dy(III) in a nitric acid medium. The influences of solid-to-liquid ratio, pH, contact time, temperature, and initial concentration on the adsorption behavior of the D001 resin were investigated through batch experiments. The applicability of the resin in simulated feed solutions was verified via dynamic column experiments. The adsorption mechanism was elucidated using Fourier transform infrared

spectroscopy (FT-IR) and X-ray photoelectron spectroscopy (XPS). This study significantly suppressed the adsorption of Co(II), thereby enabling the efficient, single-step separation of Nd(III) and Dy(III) from the Co-Nd-Dy ternary system. This work lays a foundation for the subsequent individual separation of Nd(III) and Dy(III), demonstrating promising application potential.

2. Materials and Methods

2.1. Materials and Reagents

The styrene-based macro-porous strong-acid cation exchange resin D001 was supplied by Jiangsu Suqing Water Treatment Engineering Group Co., Ltd. (Jiangyin, China), with a particle size of 0.315–1.25 mm, a moisture content of 45–50%, and a volume exchange capacity of ≥1.8 eq/L. $Co(NO_3)_2{\cdot}6H_2O$ (AR ≥ 99%) was provided by Guangdong Guanghua Sci-Tech Co., Ltd. (Shantou, China). $Nd(NO_3)_3{\cdot}6H_2O$ (AR ≥ 99%) and $Dy(NO_3)_3{\cdot}5H_2O$ (AR ≥ 99%) were supplied by Shanghai Aladdin Biochemical Technology Co., Ltd. (Shanghai, China). All inorganic/organic reagents and certain metal chlorides used in this study, including ethanol (C_2H_5OH, AR), sodium hydroxide (NaOH, AR), sodium chloride (NaCl, AR), ammonia solution ($NH_3{\cdot}H_2O$, AR), ethylenediaminetetraacetic acid (EDTA, AR), phosphoric acid (H_3PO_4, AR), hydrochloric acid (HCl, AR), ammonium chloride (NH_4Cl, AR), and sulfuric acid (H_2SO_4, AR), were purchased from Sinopharm Chemical Reagent Co., Ltd. (Shanghai, China).

2.2. Material Pretreatment

The D001 resin particles were placed in a 500 mL beaker, followed by the addition of an ethanol solution while stirring. This washing step was repeated three times. Subsequently, the material was rinsed three times with deionized water to remove organic impurities. Finally, the resin was transferred to a culture dish, covered with perforated plastic wrap, and dried in an oven at 60 °C for 24 h to prepare it for subsequent adsorption experiments.

2.3. Static Adsorption Experiment

A mixed solution containing Co(II), Nd(III), and Dy(III) at concentrations of 500 mg/L each was prepared using cobalt nitrate hexahydrate, neodymium nitrate hexahydrate, dysprosium nitrate pentahydrate, and deionized water. The solution pH was adjusted with nitric acid and sodium hydroxide to simulate the adsorption feed solution. In each adsorption experiment, 0.1 g of adsorbent and 0.02 L of the mixed solution were placed in a 50 mL glass vial and agitated in a thermostatic shaker at 25 °C with a shaking speed of 140 rpm. After reaching the predetermined adsorption time, solid–liquid separation was carried out using a 5 mL syringe. The concentrations of metal ions in the supernatant were then determined by inductively coupled plasma atomic emission spectrometry (ICP-OES). The adsorption capacity Q (mg/g), adsorption efficiency E (%), desorption capacity Q_d (mg/g), and desorption efficiency E_d (%) were calculated according to the following formulas (Equations (1)–(4)):

$$Q = \frac{(C_0 - C)}{m} \times V \quad (1)$$

$$E = \frac{(C_0 - C)}{C_0} \times 100\% \quad (2)$$

$$Q_d = C_d \times \frac{V}{m} \quad (3)$$

$$E_d = \frac{Q_d}{Q} \times 100\% \quad (4)$$

Here, C_0 and C (mg/L) represent the concentrations of Co, Nd, and Dy ions before and after adsorption, respectively. C_d (mg/L) is the concentration of metal cations in the solution after desorption. V (L) and m (g) denote the volume of the solution and the mass of the adsorbent, respectively.

2.4. Analytical Methods

The concentrations of metal ions were quantitatively analyzed using inductively coupled plasma optical emission spectrometry (ICP-OES, ICPS-7510, Shimadzu, Kyoto, Japan). The morphological structure and elemental distribution of the D001 resin were observed using field emission scanning electron microscopy (SEM-EDS, S-3400N, Hitachi, Tokyo, Japan). Thermal stability data for the resin were obtained using simultaneous thermogravimetric-differential scanning calorimetry (TG-DSC, STA 449 F3, NETZSCH, Selb, Germany) under a nitrogen (N_2) atmosphere. The temperature range was 25–800 °C with a heating rate of 10 °C/min. The specific surface area and average pore diameter of the resin were measured using a surface area analyzer (BET, TriStar II 3020, Micromeritics, Norcross, GA, USA) under a nitrogen atmosphere. The surface potential of the resin was measured using a Zeta potential analyzer (NanoBrook Omni, Brookhaven Instruments, Holtsville, NY, USA). The types of surface functional groups on the resin were analyzed using Fourier transform infrared spectroscopy (FTIR, Thermo Fisher Scientific Nicolet iN10, Thermo Fisher Scientific, Waltham, MA, USA) in the wavenumber range of 400–4000 cm^{-1}. Changes in elemental composition and functional groups before and after adsorption were investigated using X-ray photoelectron spectroscopy (XPS, Thermo Scientific K-Alpha, Thermo Fisher Scientific, Waltham, MA, USA).

2.5. Column Separation Experiment

Dynamic adsorption was performed by packing 2.5 g of D001 resin into a chromatographic column (Φ × h: 1 cm × 10 cm, flow rate: 10 mL/h). The effluent was collected at room temperature using a fraction collector (Model No. 47199, Shanghai Jiapeng Technology Co., Ltd., Shanghai, China). After pre-equilibration, the simulated Co-Nd-Dy feed solution was passed through the column until the ion concentration in the collected effluent approached that of the feed solution. Subsequently, the column was rinsed with ultrapure water to remove any residual solution. Finally, 2.5 mol/L H_2SO_4 was introduced as the eluent to desorb the adsorbed metal ions from the resin.

3. Results and Discussion

3.1. Characterization

The surface morphology and elemental distribution of the material were obtained by SEM-EDS, as shown in Figure 1a,b. D001 is a macro-porous strong-acid cation exchange resin with a styrene-based matrix and $–SO_3^-$ as the characteristic functional groups, where Na^+ is ionically bonded to $–SO_3^-$ to form sodium sulfonate ($–SO_3Na$). The D001 resin exhibits smooth surfaces and regularly shaped spherical particles without obvious fragmentation or surface defects, with a dense internal structure. Energy-dispersive X-ray spectroscopy (EDS) analysis indicates that the resin is primarily composed of carbon (C), oxygen (O), sulfur (S), and sodium (Na).

The thermal stability of D001 was determined using TG-DSC, with the results presented in Figure 1c. In the temperature range of 25–220 °C, a weight loss of approximately 8% occurred, accompanied by an endothermic peak in the DSC curve, which corresponds to the evaporation of water molecules from the material surface [28]. As the temperature increased further, the material continued to lose mass, showing a weight loss of about 5% between 150–380 °C. An exothermic peak appeared in the DSC curve at 380 °C, attributable

to the decomposition of the characteristic sulfonate groups ($–SO_3^-$) of the D001 resin [29]. Upon further heating, a sharp weight loss of approximately 16% occurred, accompanied by a major exothermic DSC peak in the range of 400–430 °C, marking the main stage of rapid breakdown and oxidation of the poly(styrene-divinylbenzene) backbone of the material [30]. Finally, a gradual weight loss of around 20% was observed, resulting from the oxidation of sulfur residues and deep carbonization of the carbonaceous skeleton. The total weight loss reached about 50%, indicating that the thermal stability limit of the resin in air is approximately 300 °C. Beyond this temperature, the decomposition of $–SO_3^-$ groups leads to the loss of ion exchange functionality.

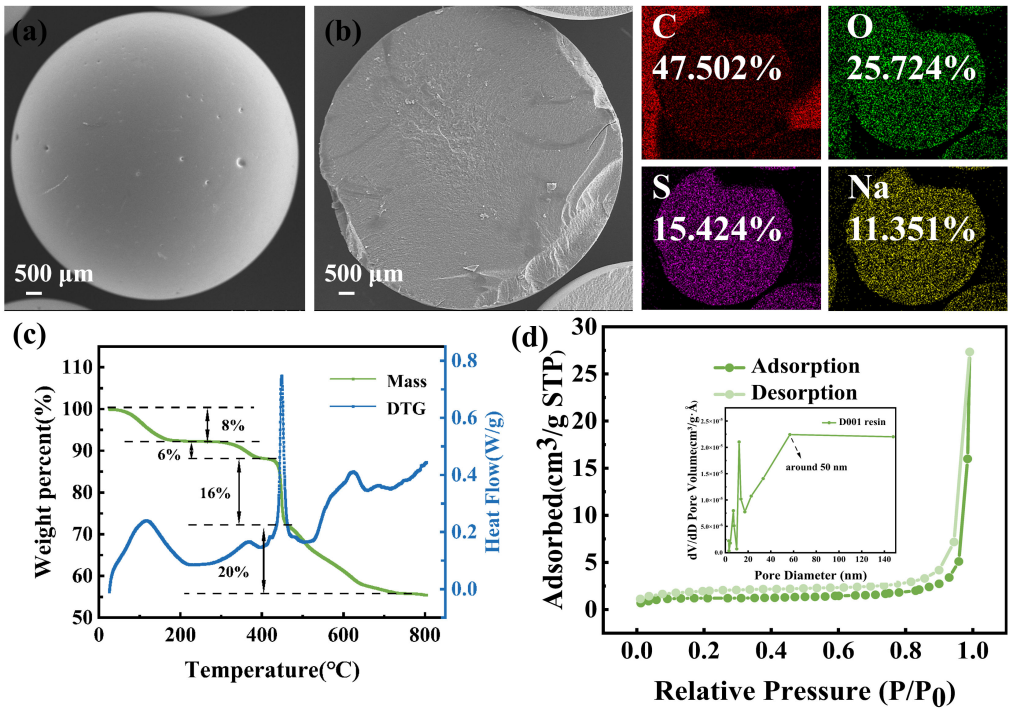


Figure 1. (**a**) SEM images of the surface, (**b**) EDS images, (**c**) thermogravimetric analysis curve of D001 resin under N_2 atmosphere, and (**d**) N_2 adsorption–desorption isotherms and pore size distributions.

The pore structure and specific surface area information of D001 were obtained from N_2 adsorption–desorption isotherms, as shown in Figure 1d. Prior to the measurement, the sample was degassed under vacuum at 80 °C for 12 h to remove any adsorbed moisture and impurities. The pore size distribution of D001 resin exhibits a unimodal shape, with the primary peak located in the range of 30–80 nm and a peak pore diameter around 50 nm. Almost no signal is detected in the region below 10 nm, indicating the absence of micropores (<2 nm) and mesopores (2–10 nm) in the material. This macro-porous structure facilitates the rapid diffusion of rare earth ions (Nd(III) and Dy(III)) and transition metal ions (Co(II)) within the particles, reducing liquid film diffusion resistance [31]. The isotherm of the material belongs to a typical type IV(a) pattern [32], with adsorption capacity approaching zero in the low relative pressure region ($P/P_0 < 0.1$), further confirming the lack of micropores. In the medium relative pressure range, an H3/H4 [33] mixed-type hysteresis loop appears, where the desorption branch lies to the left of the adsorption branch.

3.2. Batch Adsorption Experiment

3.2.1. Effect of Solid-Liquid Ratio on Adsorption Capacity

The effect of the solid-to-liquid ratio on the adsorption capacity of the resin for Co-Nd-Dy is shown in Figure 2a. As the solid-to-liquid ratio increased from 0.5 to 10 g/L, the adsorption capacities for Nd(III) and Dy(III) initially rose rapidly and then decreased

gradually. Under a low solid-to-liquid ratio (0.5 g/L), the adsorption capacity was high, but this would lead to waste of the ion feed solution. At 10 g/L, particle aggregation reduced the effective adsorption area and lowered the liquid film mass transfer coefficient, resulting in inefficient use of the adsorbent [34]. Considering both cost and adsorption performance, a solid-to-liquid ratio of 5 g/L (0.1 g/20 mL) was selected. At this ratio, the adsorption capacities for Co(II), Nd(III), and Dy(III) were maintained at 15 mg/g, 85 mg/g, and 79 mg/g, respectively, achieving an optimal balance between adsorbent dispersion and mass transfer flux.

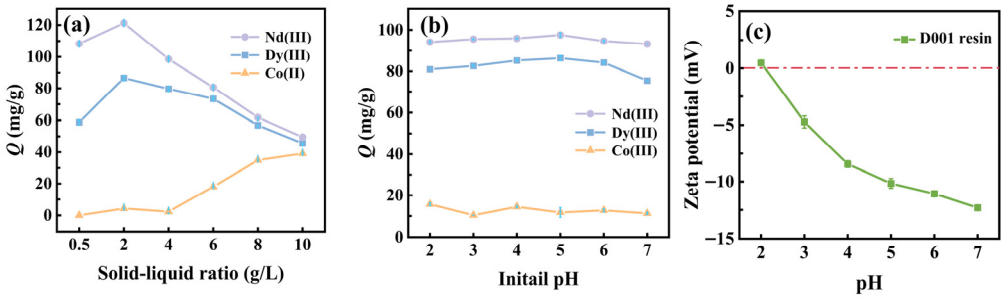


Figure 2. (**a**) Effect of solid-to-liquid ratio on adsorption capacity. (**b**) Effect of initial pH on adsorption capacity. (**c**) Zeta potential on the surface of D001 resin (m/V = 5 g/L, T = 298 K, C_0 = 500 mg/L, and t = 12 h).

3.2.2. Effect of pH on Adsorption

To investigate the maximum equilibrium adsorption capacity of the D001 resin for Co(II), Dy(III), and Nd(III) and to optimize the separation conditions, this study measured the equilibrium adsorption capacities of the resin for each metal ion under different initial pH conditions (2–7), as shown in Figure 2b. The adsorption capacities of the three ions showed little variation in response to changes in pH. Across the entire pH range, the resin exhibited a strong affinity for Dy(III) and Nd(III), with their adsorption capacities being significantly higher than that of Co(II). Within the pH range of 2.0 to 5.0, the adsorption capacities increased rapidly, after which the rate of increase gradually slowed. At pH < 4.0, although the adsorption capacity for Co(II) remained very low, the adsorption of Dy/Nd was also insufficient, resulting in an unsatisfactory overall recovery rate. Based on a comprehensive analysis, at pH 5, the adsorption capacities for Dy(III) and Nd(III) reached their maximum values of 86.381 mg/g and 97.566 mg/g, respectively, representing the optimum condition for achieving efficient separation. At this pH, the adsorption of Co(II) remained effectively suppressed, thereby achieving optimal separation between Co(II) and the rare earth elements. Consequently, all subsequent experiments were conducted under an initial pH condition of 5.

To understand the surface charge characteristics of the D001 resin, the zeta potential of the material was measured, as shown in Figure 2c. The surface charge of the resin shifted from positive to negative over the pH range of 2 to 7, yet the adsorption capacity varied only slightly across this pH range, indicating that the adsorption is controlled by ion exchange at the adsorption sites of the resin. The adsorption capacity of Co(II) remained consistently much lower than that of Dy(III) and Nd(III). The fundamental reason lies in the difference in ion charge density: Co is a divalent ion, whereas Dy and Nd are trivalent ions. At the strongly negatively charged $–SO_3^-$ sites on the resin, trivalent ions with higher charge density experience stronger electrostatic attraction and binding energy, thus holding an absolute advantage in ion exchange competition [27].

3.2.3. Adsorption Kinetics Study

To understand the adsorption kinetics of the resin for Nd(III), Dy(III), and Co(II), adsorption experiments were conducted over a time range of 5–720 min at temperatures of 298 K, 308 K, and 318 K. The results are shown in Figure 3a,b for Nd(III) and Dy(III), and in Figure 3c for Co(II). The kinetic curves clearly illustrate that the adsorption capacities for Nd(III) and Dy(III) increased rapidly and then gradually approached equilibrium, reaching adsorption equilibrium within 90 min. Nd(III) and Dy(III) exhibited overlapping adsorption profiles across the tested temperatures, which can be attributed to their similar valence states, ionic properties, and ion exchange mechanisms. These similarities reduced the influence of differences in ionic radius (Nd(III): 0.0983 nm, Dy(III): 0.0912 nm [35]), ultimately resulting in highly consistent kinetic behavior. In contrast, the adsorption kinetics of Co(II) exhibited a distinctly different trend. The adsorption capacity of Co(II) initially increased within the first 10 min, reaching approximately 25.0 mg/g at 298 K and 308 K, and 27.0 mg/g at 318 K. However, beyond 10 min, the adsorbed amount of Co(II) gradually declined, eventually stabilizing at around 11.5–13.5 mg/g after 120 min across all temperatures. This unusual decrease may be attributed to competitive adsorption or displacement effects within the ternary metal system, where Nd(III) and Dy(III), which have higher affinities for the active sites of D001 resin, gradually replace the initially adsorbed Co(II) [36]. The final low adsorption capacity of Co(II) (less than 14 mg/g) confirms the high selectivity of D001 resin for Nd(III) and Dy(III) over Co(II) under the experimental conditions (m/V = 5 g/L, C_0 = 500 mg/L, pH = 5).

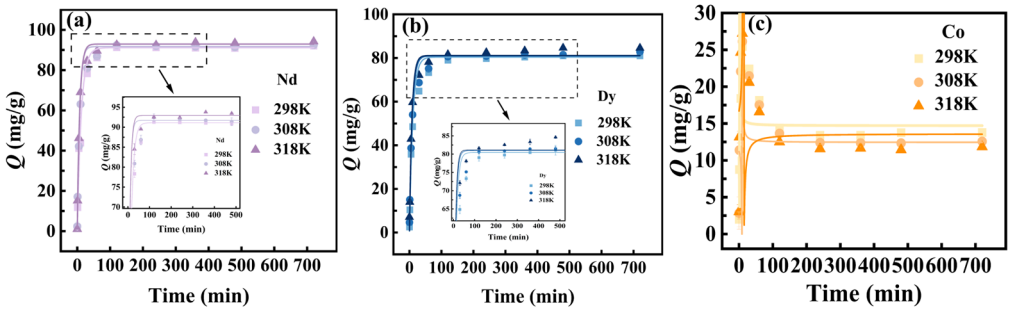


Figure 3. Adsorption kinetics of Nd(III) (**a**), Dy(III) (**b**), and Co(II) (**c**) at different temperatures (298 K, 308 K, and 318 K). The inset shows a magnified section. (m/V = 5 g/L, T = 298 K–318 K, C_0 = 500 mg/L, and pH = 5).

This study employed the pseudo-first-order (PFO) [37], pseudo-second-order (PSO) [38], and Weber–Morris (W-M) [39] intra-particle diffusion models to fit the adsorption kinetics in Equations (S1)–(S3). The evaluation of the adsorption kinetic models was based on three key statistical parameters: (i) probability > F-value (Prob > F), (ii) coefficient of determination (R^2), and (iii) residual sum of squares (RSS). The kinetic fitting parameters are summarized in (Tables S1 and S2). and the corresponding kinetic fitting curves are presented in Figure 4a–i.

The Prob > F significance level is used to assess how well the sample results represent the overall population and the accuracy of the test data. If Prob > F is less than 0.05, the model is considered to describe the data trend with statistical significance. As shown in Supplementary Materials Tables S1 and S2, the Prob > F values of the PSO model are lower than those of the PFO model, indicating stronger statistical validity for the PSO model. Furthermore, the PSO model exhibits a lower RSS and demonstrates nearly perfect goodness-of-fit (R^2 > 0.999) across all temperatures, suggesting that the overall adsorption process is predominantly governed by a chemisorption mechanism. For Co(II), the kinetic parameters obtained from the three models are summarized in Table S3. The PSO model

also provided the best fit for Co(II) adsorption, with R^2 values exceeding 0.998 across all temperatures—comparable to the fitting results obtained for Nd(III) and Dy(III). However, it is worth noting that the PSO rate constant (K_2) for Co(II) exhibited negative values at all temperatures, which is physically unrealistic and further confirms that Co(II) adsorption does not follow a typical uptake process. This anomalous behavior is consistent with the competitive adsorption and displacement effects observed in the kinetic curves, where Nd(III) and Dy(III) gradually replace the initially adsorbed Co(II) on the active sites of the D001 resin.

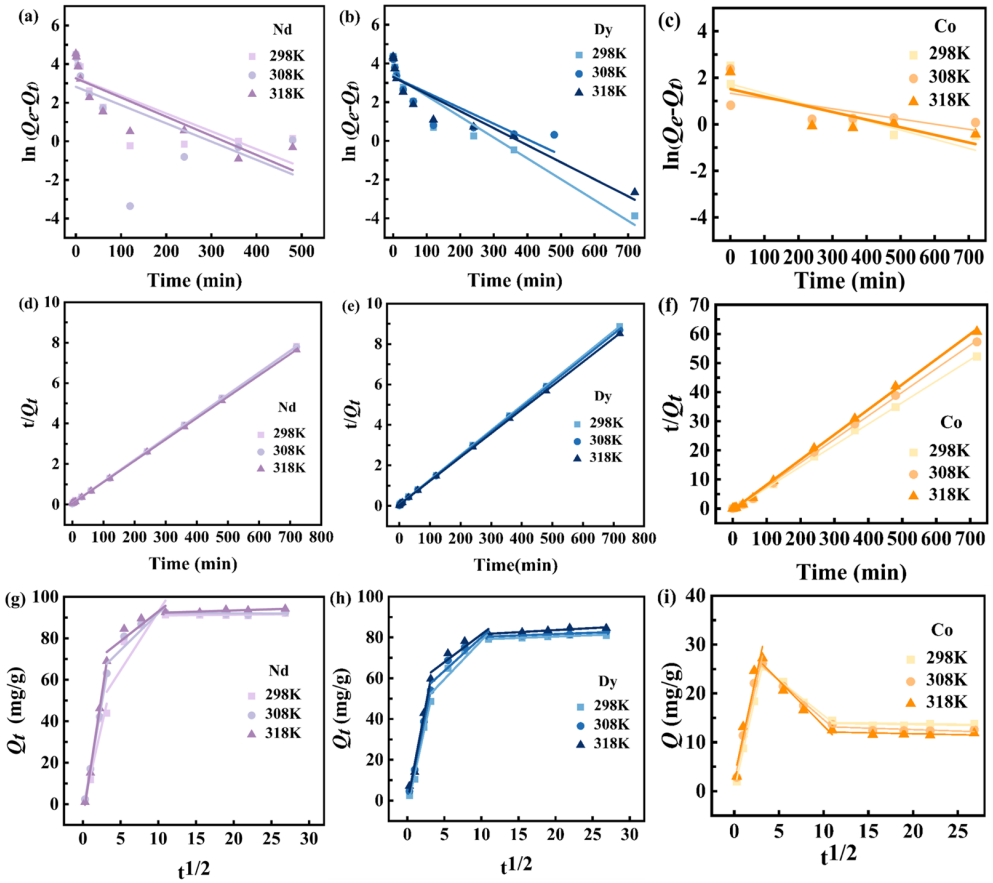


Figure 4. Pseudo-first-model of Nd(III) (**a**), Dy(III) (**b**), and Co(II) (**c**). Second-order-model of Nd(III), (**d**), Dy(III) (**e**), and Co(II) (**f**). W-M model of Nd(III) (**g**), Dy(III) (**h**), and Co(II) (**i**). (m/V = 5 g/L, T = 298 K-318 K, C_0 = 500 mg/L, and pH = 5).

Simultaneously, the fitting results of the W-M model confirm the presence of intra-particle diffusion, as shown in Figure 4g,h for Nd(III) and Dy(III), and in Figure 4i for Co(II). The non-zero intercept of the fitted curve indicates that intra-particle diffusion is not the sole rate-controlling step; liquid film diffusion also plays a significant role during the initial phase. The fitting results reveal the following adsorption process: the steepest slope, observed initially, corresponds to the fastest adsorption rate due to the abundance of vacant active sites on the resin surface. Subsequently, the slope decreases significantly, indicating a slowdown in the adsorption rate as the active sites become progressively occupied by Nd(III) and Dy(III). Finally, the slope approaches zero, signaling that adsorption equilibrium has been reached. Therefore, the adsorption of Nd(III) and Dy(III) is achieved through a combined mechanism of chemisorption and internal diffusion, with chemisorption playing the dominant role [40].For Co(II), the W-M model fitting results exhibited a distinctly different pattern. In contrast to the typical three-stage adsorption process observed for Nd(III) and Dy(III), the intraparticle diffusion plot for Co(II) showed an initial increase

followed by a gradual decline, which is consistent with the competitive adsorption behavior observed in the kinetic study. This unusual trend further confirms that Co(II) adsorption is not a simple uptake process; rather, it involves displacement by Nd(III) and Dy(III), which have higher affinities for the active sites of the resin. The non-linear and decreasing trend in the W-M plot suggests that intraparticle diffusion is not the dominant rate-controlling mechanism for Co(II). Instead, the adsorption process appears to be governed primarily by surface interactions and competitive effects within the ternary metal system.

3.2.4. Adsorption Isotherm Study

To investigate the adsorption behavior of D001 resin for Nd(III) and Dy(III), adsorption isotherms were determined under conditions of initial pH 5, a solid-to-liquid ratio of 5 g/L, and an adsorption time of 12 h. The experiments were conducted at three temperatures—298 K, 308 K, and 318 K—with initial concentrations ranging from 300 to 3000 mg/L, as shown in Figure 5a,b. The results indicate that the adsorption capacity increased rapidly with rising equilibrium concentration, then gradually slowed down, and finally reached saturation. In the low equilibrium concentration range, the large concentration gradient acted as the driving force, enabling ions to efficiently overcome liquid film diffusion resistance and quickly occupy the abundant vacant sites on the resin surface, leading to a sharp increase in adsorption capacity. As the concentration continued to increase, the active sites on the resin surface approached saturation, resulting in a gradual approach to adsorption equilibrium. At this stage, the saturated adsorption capacities for Nd(III) and Dy(III) were 135.668 mg/g and 95.377 mg/g at 298 K; 143.006 mg/g and 111.132 mg/g at 308 K; and 154.983 mg/g and 120.958 mg/g at 318 K.

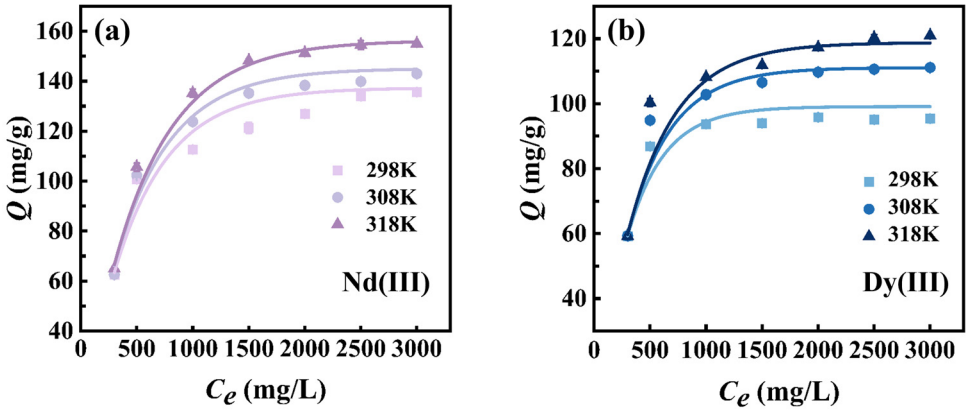


Figure 5. (**a**) Adsorption isothermal of Nd(III). (**b**) Adsorption isothermal of Dy(III) (m/V = 5 g/L, T = 298 K–318 K, C_0 = 500 mg/L, pH = 5, and t = 12 h).

To gain deeper insight into the adsorption behavior of Nd(III) and Dy(III), the adsorption isotherms were fitted using the Langmuir [41], Freundlich [42], Temkin [43], and Dubinin–Radushkevich (D-R) [44] models (Equations (S4)–(S8)). Adsorption isotherm studies were conducted by mixing 0.1 g of D001 resin with 0.02 L of ternary metal ion solution (containing Co(II), Nd(III), and Dy(III), each at an initial concentration of 500 mg/L), corresponding to a solid-to-liquid ratio of 5 g/L. The fitting results are shown in Figure 6a–h, and the corresponding kinetic parameters are summarized in Tables S3 and S4. For Nd(III), the R^2 values of the Langmuir model at 298 K, 308 K, and 318 K were 0.9971, 0.9956, and 0.9941, respectively—all above 0.99 and significantly better than those of the Freundlich (R^2~0.85) and Temkin (R^2~0.91) models. Moreover, the Langmuir model exhibited lower Prob > F values and smaller RSS. For Dy(III), the Langmuir model also showed the highest R^2 values (0.9976, 0.9969, and 0.9961, respectively), along with lower Prob > F values and RSS compared to the other models. These results indicate that the adsorption isotherm

data are in strong agreement with the Langmuir model, revealing a monolayer adsorption mechanism of D001 resin for Nd(III) and Dy(III) [45].

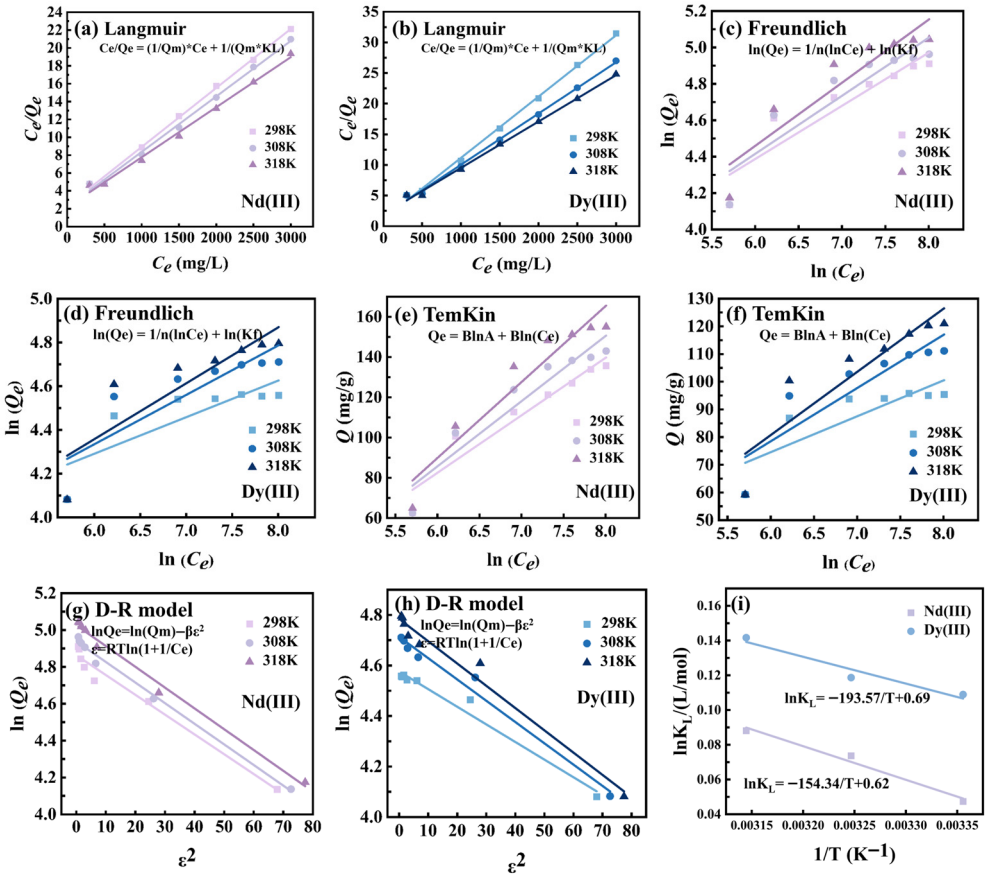


Figure 6. (**a**) Langmuir model of Nd(III). (**b**) Langmuir model of Dy(III). (**c**) Freundlich model of Nd(III). (**d**) Freundlich model of Dy(III). (**e**) Temkin model of Nd(III). (**f**) Temkin model of Dy(III). (**g**) Dubinin–Radushkevich of Nd(III). (**h**) Dubinin–Radushkevich of Dy(III). (**i**) Thermodynamics of Nd(III) and Dy(III) at different temperatures (m/V = 5 g/L, T = 298 K–318 K, C_0 = 500 mg/L, pH = 5, and t = 12 h).

The van't Hoff equation (provided in Equations (S9)–(S11)) was used to determine the thermodynamic parameters of adsorption, including the enthalpy change (ΔH°, J/mol), entropy change (ΔS°, J/mol·K), and Gibbs free energy change (ΔG°, J/mol), as shown in Figure 6i and Table 1. ΔH° reflects the temperature dependence of adsorption, ΔS° characterizes the entropy change of the system during adsorption, and ΔG° indicates the change in free energy, governing the spontaneity of the adsorption process [46]. The results show ΔH° > 0, ΔS° > 0, and ΔG° < 0, indicating that the adsorption of Nd(III) and Dy(III) by the resin is an endothermic and spontaneous process.

Table 1. Thermodynamic parameters of Nd(III) and Dy(III) at different temperatures.

Element	T (K)	ΔG^0 (J/mol)	ΔH^0 (J/mol)	ΔS^0 (J/mol K)
Nd	298	−125	160.9	5.82
	308	−184		
	318	−241		
Dy	298	−253	128.3	5.14
	308	−304		
	318	−356		

3.2.5. Desorption Performance and Stability of the Resin

The desorption performance was evaluated, as shown in Figure 7a. Ten different eluents were assessed for their effectiveness in desorbing Co(II), Nd(III), and Dy(III). Strong acidic eluents, such as HCl, H_2SO_4, and HNO_3, demonstrated significantly higher desorption efficiencies for Nd(III) and Dy(III) compared to other reagents. In contrast, the desorption rates for Co(II) were generally low, consistent with its relatively weak adsorption affinity on the D001 resin. Considering both desorption efficiency and the avoidance of introducing new metal ions, H_2SO_4 was selected as the eluent.

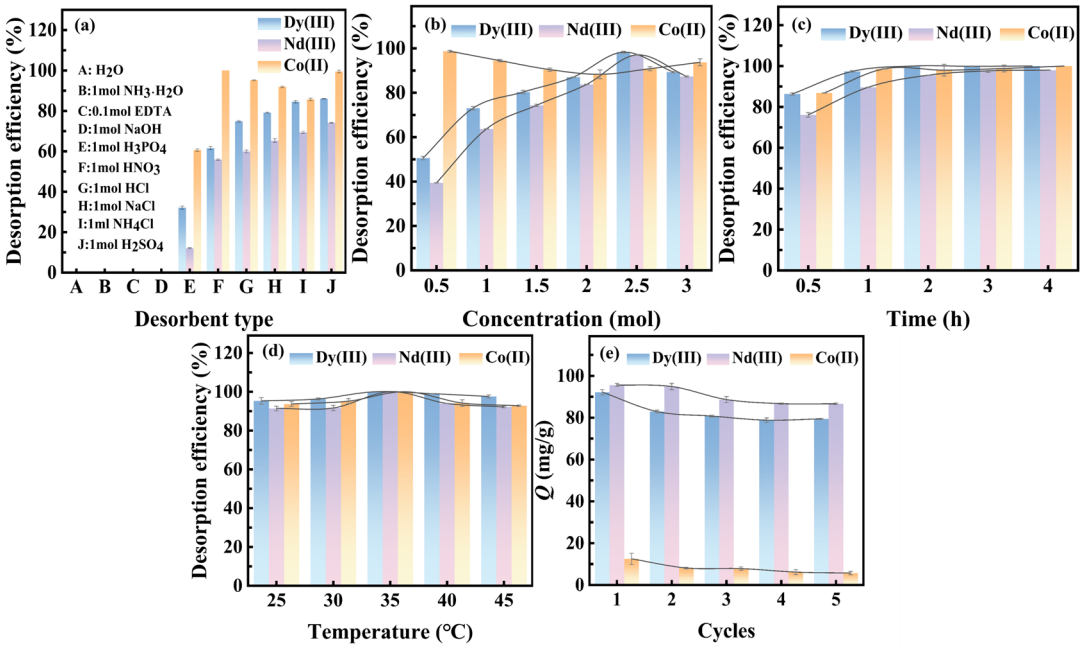


Figure 7. (**a**) Desorption effects of different eluents on Nd(III), Dy(III), and Co(II). (**b**) Effect of different H_2SO_4 concentrations on desorption performance. (**c**) Effect of desorption time on desorption performance. (**d**) Effect of desorption temperature on desorption performance. (**e**) Reusability of the D001 resin (m/V = 5 g/L, T = 298 K, C_0 = 500 mg/L, pH = 5, and t = 12 h).

To further optimize the desorption performance, the effects of H_2SO_4 concentration, time, and temperature on desorption were investigated, as shown in Figure 7b–d. It was observed that as the acid concentration increased to 2.5 M, the desorption rates of both Nd(III) and Dy(III) reached their peak values. The desorption process was completed rapidly within the first hour and then gradually approached equilibrium. Temperature showed no significant effect on the desorption performance.

To evaluate the cycling stability of the resin, adsorption–desorption cycling experiments were conducted, with the results shown in Figure 7e. Over five consecutive cycles, the adsorption capacities of the D001 resin for Nd(III) and Dy(III) remained at high levels, with only a slow decline, demonstrating the resin's good structural stability and reusability. Overall, the D001 resin exhibits efficient desorption and stable cycling performance for Nd(III) and Dy(III) under strong acidic elution conditions.

3.2.6. Column Experiments

The practical applicability of the resin was further assessed through chromatographic column separation experiments, as shown in Figure 8a,b. In the initial loading stage (Phase A), the resin exhibited excellent ion selectivity: Nd(III) and Dy(III) were rapidly immobilized at the front section of the column bed, while the majority of Co(II) remained unadsorbed, resulting in the early elution of high-purity Co(II) in the initial effluent fraction.

The effluent collected during this phase allowed for the recovery of Co(II) with a purity of 99.99%. In Phase B and beyond, as the column bed approached saturation for Nd(III) and Dy(III), the concentration of Co(II) in the effluent naturally decreased due to mass transfer processes within the column. This phenomenon does not indicate a failure in separation but rather precisely defines the operational and collection endpoint of the process: by accurately controlling the collection to Phase A, high-purity Co(II) can be separated before Nd(III) and Dy(III) break through.

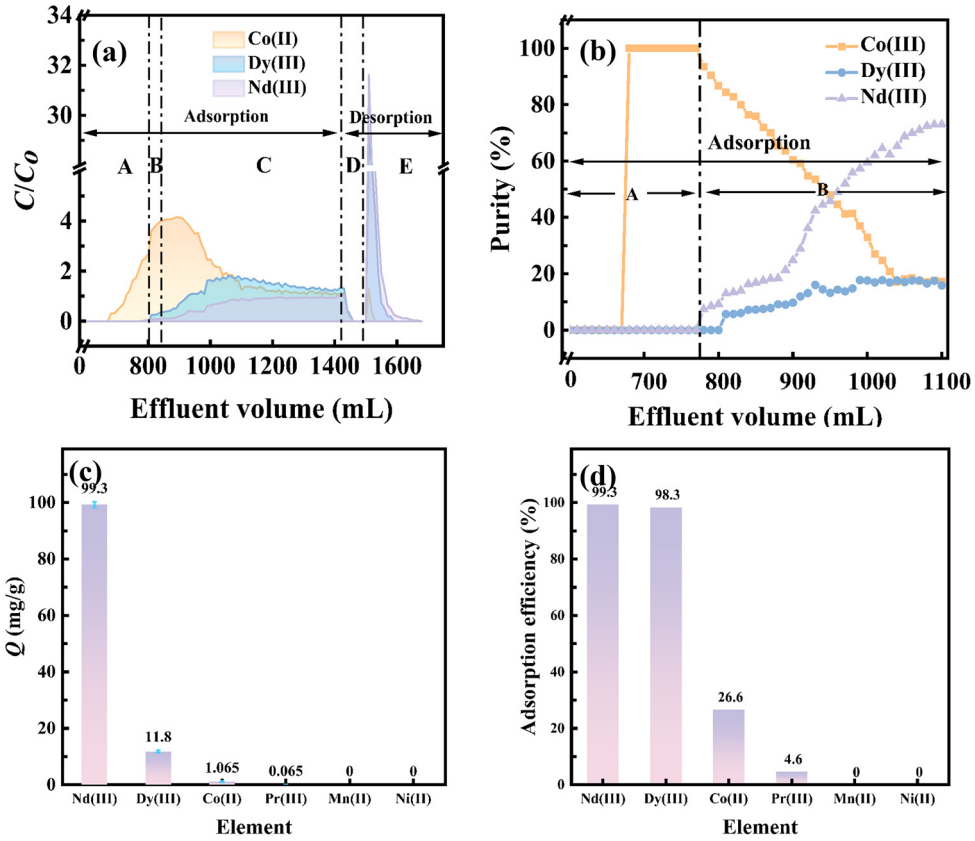


Figure 8. (**a**) Chromatographic separation of Nd(III), Dy(III), and Co(II) by D001 resin. (**b**) Purity of Nd(III) and Dy(III) in the eluent. (**c**) Selectivity of D001 resin. (**d**) Adsorption efficiency of each element (packed resin: 2.5 g, column dimension: Φ × h: 1 cm × 10 cm, T = 298 K, Nd(III): 500 mg/L, Dy(III): 60 mg/L, Co(II): 20 mg/L, Pr(III): 7 mg/L, Mn(II): 1 mg/L, and Ni(II): 0.39 mg/L).

In summary, this study successfully confirms the feasibility of using D001 resin for the separation of the Co-Nd-Dy ternary system. Its key advantage lies in the ability to achieve direct separation of Co(II) from Dy(III) and Nd(III) at the front end of the process through a straightforward dynamic adsorption operation.

3.2.7. Adsorption Selectivity

In a multi-ion competitive system simulating the actual composition of an NdFeB permanent magnet waste leachate (where Fe(III) and Al(III) have completely precipitated at pH 6), containing Nd(III): 500 mg/L, Dy(III): 60 mg/L, Co(II): 20 mg/L, Pr(III): 7 mg/L, Mn(II): 1 mg/L, and Ni(II): 0.39 mg/L, the selective adsorption characteristics of D001 resin were systematically investigated, as shown in Figure 8c. Experiments demonstrated that under conditions of solid-to-liquid ratio of 0.1 g/20 mL, pH 5, 298 K, and adsorption for 12 h, the adsorption capacity of the material for Nd(III) reached 99.3 mg/g, and for Dy(III) it was 11.8 mg/g, both significantly higher than that for Co(II) (1.065 mg/g). In contrast, almost no adsorption was observed for Pr(III), Mn(II), and Ni(II) (all $\leq$ 0.1 mg/g). The

adsorption efficiencies of Nd and Dy are also significantly higher than those of the other competing ions, as shown in Figure 8d. These findings confirm the resin's outstanding selectivity for Dy(III) and Nd(III).

3.3. Adsorption Mechanism Study

3.3.1. SEM-EDS Analysis

The SEM-EDS analysis of the D001 resin after adsorption of Nd(III) and Dy(III) is shown in Figure 9a. EDS analysis confirmed that its primary constituent elements remain C, O, S, and Na. In the EDS spectrum of the resin after adsorption, significant signals of Nd(III) and Dy(III) were clearly detected along with a weak signal of Co(II), verifying the successful separation of Nd(III) and Dy(III) from the solution. Simultaneously, compared to the resin before adsorption, the relative contents of the C, O, and Na elements in the resin after adsorption were significantly reduced. This reduction indicates that oxygen- and sodium-containing elements are involved in the adsorption mechanism, likely through cation exchange.

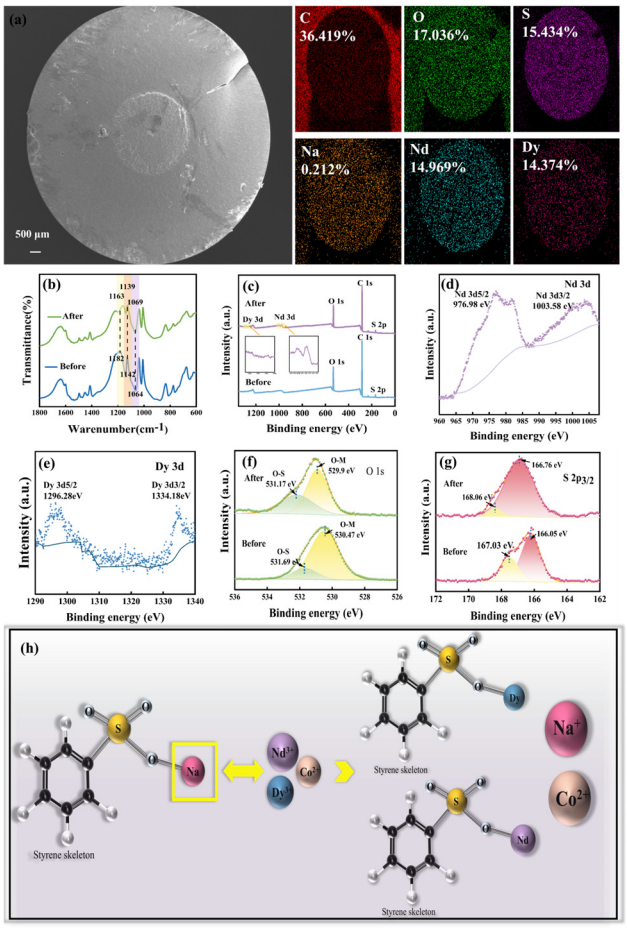


Figure 9. (**a**) SEM and EDS images of Nd-Dy-loaded D001 resin, (**b**) FT-IR spectra of D001 resin before and after adsorption, (**c**) XPS spectra of the resin before and after adsorption, and (**d**–**g**) respectively represent the XPS spectra of Nd 3d, Dy3d O 1s, and S 2p3/2. (**h**) Adsorption mechanism of D001 resin.

In summary, the discrepancy between the minor variation in adsorption capacity and the significant change in zeta potential confirms the dominance of the ion exchange mechanism. Meanwhile, the substantial difference in adsorption capacity between Co(II) and Dy(III)/Nd(III) directly originates from the intrinsic advantage of trivalent rare earth ions in electrostatic interactions, fundamentally ensuring the efficient separation of Co(II) from Nd(III) and Dy(III).

3.3.2. FI-IR Analysis

Fourier transform infrared spectroscopy (FTIR) analysis was employed to characterize the functional group transformation and chemical bond changes of the D001 resin before and after adsorption, as shown in Figure 9b. Prior to adsorption, the D001 resin exhibited strong peaks at 1182 cm^{-1} and 1142 cm^{-1}, corresponding to the asymmetric stretching vibrations of the S=O bonds [47], while the peak at 1064 cm^{-1} was mainly attributed to the symmetric stretching vibration of the S–O bond [48]. After adsorption, these characteristic peaks systematically shifted: the S=O vibration peaks at 1182 cm^{-1} and 1142 cm^{-1} shifted to lower wavenumbers at 1163 cm^{-1} and 1139 cm^{-1}, respectively, and the S–O vibration peak at 1064 cm^{-1} shifted to a higher wavenumber at 1069 cm^{-1}. The red shift of the S=O peaks indicates a decrease in electron cloud density and weakening of bond strength in the S=O double bonds, resulting from the coordination of Nd(III) and Dy(III) with the O atoms of $–SO_3^-$, which draws electron density toward the metal ions [49]. The blue shift of the S–O peak reflects increased rigidity of the S–O single bond, associated with the transformation of $–SO_3^-$ into a metal-salt-like structure [50,51]. These observations confirm the coordination binding of Dy(III) and Nd(III) with the sulfonate groups on the resin.

3.3.3. XPS Analysis

XPS full-spectrum and fine-spectrum analyses further confirmed the adsorption mechanism at the elemental composition and chemical state levels. As shown in Figure 9c, the XPS full spectrum displayed characteristic peaks of C 1s, O 1s, and S 2p. After adsorption, new characteristic peaks corresponding to Nd 3d and Dy 3d appeared, directly confirming the successful loading of rare earth ions onto the resin surface. Detailed spectra of Nd and Dy are shown in Figure 9d,e. The binding energies of Nd $3d_5/_2$ and Nd $3d_3/_2$ were 976.98 eV and 1003.58 eV, respectively, while those of Dy $3d_5/_2$ and Dy $3d_3/_2$ were 1296.28 eV and 1334.18 eV, respectively. The O 1s fine spectrum in Figure 9f shows that after adsorption, the peak assigned to the S–O bond in $–SO_3^-$ (O–S) shifted significantly from 531.17 eV to 531.69 eV, with an increase in binding energy. The peak attributed to metal oxides (O–M) also shifted from 529.9 eV to 530.47 eV [52]. These changes collectively indicate an overall reduction in the electron cloud density around O atoms after adsorption, primarily due to the formation of coordination bonds (M–O) between the O atoms as electron donors and Nd(III) and Dy(III) ions, leading to electron transfer toward the metal ions [53]. In the S 2p fine spectrum shown in Figure 9g, the S 2p3/2 peak shifts from 167.03 eV to 168.06 eV, which further confirms that the electron cloud around the sulfur atom is pulled away due to the participation of $–SO_3^-$ in coordination, resulting in an increase in its binding energy [54].

The XPS data further corroborate the conclusions drawn from FT-IR, revealing the ion exchange mechanism between Nd(III)/Dy(III) and the $–SO_3^-$ groups of the D001 resin, as shown in Figure 9h. Nd(III) and Dy(III) replace Na^+ through electrostatic and coordination interactions, forming M–O–S bonds with the O atoms of $–SO_3^-$. The formation of these bonds leads to a decrease in the electron cloud density of the S=O double bond (resulting in the red shift of the S=O peak in FT-IR and the increase in binding energy of O and S in XPS), while simultaneously altering the vibrational environment of the sulfonate group (causing the blue shift of the S–O peak in FT-IR).

3.3.4. Comparison with Other Reported Adsorbents

To further assess the performance of D001 resin within the framework of existing separation technologies, a comparative overview of recently reported adsorbents and methods for the separation of Nd(III), Dy(III), and Co(II) is provided. The comparison

highlights key performance indicators, including adsorption capacity, kinetics, reusability, applicable pH range, and selectivity toward Co separation.

As shown in Table 2, D001 resin exhibits several distinct advantages over other reported materials. When compared with other reported materials, such as amorphous tin phosphate (am-SnP) [55] and 3D-printed aminophosphonate filters [56], D001 resin exhibits substantially higher adsorption capacities for Nd(III) (154.98 mg/g at 318 K) and Dy(III) (120.96 mg/g at 318 K), while performing comparably to DPPA/CaALG hydrogel [19] under mild pH conditions (pH 5). More importantly, D001 reaches adsorption equilibrium within 90 min, which is considerably faster than most other adsorbents, reflecting its superior mass transfer efficiency and practical applicability.

Table 2. D001 resin compared to other reported adsorbents.

Adsorbent	Saturated Adsorption Capacity (mg/g)	Adsorption Kinetics (Equilibrium Time)	Reusability	Applicable Acidity/pH	Selectivity for Co
D001 resin (This work)	Nd:154.98 (318 K) Dy:120.96 (318 K)	90 min	Nd: 86.6% Dy: 80% after 5 cycles	pH 2–7 (Wide pH range)	Adsorption efficiency: Nd 99.3% Dy 98.3% Co 26.6%
Amorphous tin(IV) phosphate (am-SnP) [55]	Nd: 68.03 Dy: 58.14	Nd: 180 min Dy: 360 min	Significant decline after 2 cycles	pH 2–6 (optimum: Nd 4, Dy 3)	High selectivity ($\beta_{Nd/Co}$ up to 22.8, $\beta_{Dy/Co}$ up to 18.76)
DPPA/CaALG hydrogel [19]	Nd: 162.5 (1 M HCl) Dy: 183.5 (1 M HCl)	6 h	Dropped sharply to ~50% after 3 cycles	1 M HCl (strong acidic)	Almost no Co adsorption ($SF_{REE/Co} \geq 13{,}671$)
3D-printed aminophosphonate filter [56]	Nd: 34.6 Dy: 37.8 Y: 14.7	40 mL @ 90 mL/h (multi-step sequential)	Affected by Sc/Fe/U accumulation pre-treatment needed	pH 2 aqueous (mining wastewater)	-

Another notable advantage lies in its excellent reusability. After five consecutive adsorption–desorption cycles, D001 retains 86.6% of its initial capacity for Nd(III) and 80% for Dy(III). In contrast, DPPA/CaALG loses approximately 50% of its capacity after only three cycles [1], and am-SnP shows a marked decline after just two cycles [2]. Such robust cycling stability is essential for industrial applications, as it minimizes material replacement costs and ensures long-term process reliability.

In addition, D001 operates effectively across a broad pH range of 2–7, making it adaptable to various feed compositions without the need for extensive pH adjustment. This contrasts with methods that require strongly acidic conditions (e.g., 1 M HCl for DPPA/CaALG) or non-aqueous media (e.g., PEG 200 for P350 extraction [2]), which entail additional complexity and cost.

Most importantly, unlike any of the other methods surveyed, D001 enables the one-step selective separation of Co from Nd/Dy in ternary systems. While alternative approaches focus solely on rare earth recovery or rely on multi-step processes, D001 achieves >99% Co purity in column operations through selective adsorption and displacement mechanisms.

Taken together, the combination of high adsorption capacity, rapid kinetics, excellent reusability, wide pH tolerance, and commercial availability positions D001 resin as a practical and scalable candidate for the industrial recovery of rare earth elements from NdFeB magnet leachates.

4. Conclusions

This study utilized D001 resin for the recovery of Nd(III) and Dy(III) from NdFeB simulated materials (Co-Nd-Dy ternary system). Batch experiments showed that D001 selectively separated Co(II) from Nd(III) and Dy(III) in a nitric acid environment at pH 5. Kinetic

and adsorption isotherm studies indicated that the adsorption process conformed to the pseudo-second-order kinetic model and the Langmuir isotherm model, suggesting that the adsorption of Nd(III) and Dy(III) by D001 is primarily governed by monolayer chemisorption. The saturated adsorption capacities for Nd(III) and Dy(III) reached 154.98 mg/g and 120.96 mg/g at 318 K, respectively, with stable cycling performance maintained over five consecutive adsorption–desorption cycles. The adsorption efficiencies of Nd(III) and Dy(III) were 99.3% and 98.3%, respectively, significantly higher than that of Co (26.6%). Column experiments successfully achieved separation, with Co(II) purity exceeding 99.99% after elution using 2.5 mol/L H_2SO_4. FT-IR and XPS analyses revealed that Nd(III) and Dy(III) are adsorbed via cation exchange with Na^+ on the $–SO_3Na$ groups, where S–O bonds play a critical role. The binding with rare earth ions can be represented as M–O–S (Nd–O–S and Dy–O–S). This method efficiently separates Nd(III) and Dy(III) from complex mixed solutions, demonstrating promising application potential.

Supplementary Materials: The following supporting information can be downloaded at: https://www.mdpi.com/article/10.3390/separations13030077/s1, Table S1: Kinetic parameters of PFO, PSO, and W-M adsorption models for Nd(III); Table S2: Kinetic parameters of PFO, PSO, and W-M adsorption models for Dy(III); Table S3: Kinetic parameters of PFO, PSO, and W-M adsorption models for Co(II); Table S4: Adsorption isotherm parameters of Nd(III) adsorbed by D001 resin at different temperatures; Table S5: Adsorption isotherm parameters of Dy(III) adsorbed by D001 resin at different temperatures.

Author Contributions: Methodology, Y.L., Data curation, Y.L., Writing—original draft, Y.L., Writing—review & editing, Y.L.; Methodology, H.A., Writing—review & editing, H.A., Investigation, H.A.; Methodology, Z.J., Conceptualization, Z.J., Investigation, Z.J.; Writing—review & editing, H.T., Supervision, H.T., Project administration, H.T.; Methodology, C.H., Writing—review & editing, C.H., Project administration, C.H., Funding acquisition, C.H. All authors have read and agreed to the published version of the manuscript.

Funding: This research was supported by the Central Funds Project for Guiding Local Technological Development (ZY24212006), the Guangxi Science and Technology Major Project, China (No. AA24263044, AB25069241), the Natural Science Foundation of China (No. 52364022), and the Special Fund for Science and Technology Development of Guangxi (Grant No. AD25069078).

Data Availability Statement: The original contributions presented in this study are included in the article/Supplementary Materials. Further inquiries can be directed to the corresponding author.

Conflicts of Interest: The authors Zezuo Jiang, Haixiang Tan and Chunlin He were employed by Guangxi Guosheng Rare Earth New Materials Co., Ltd., Chongzuo 532200, China. The remaining authors declare that the research was conducted in the absence of any commercial or financial relationships that could be construed as a potential conflict of interest.

References

1. Gutfleisch, O.; Willard, M.A.; Brück, E.; Chen, C.H.; Sankar, S.G.; Liu, J.P. Magnetic materials and devices for the 21st century: Stronger, lighter, and more energy efficient. *Adv. Mater.* **2011**, *23*, 821–842. [CrossRef]
2. Coey, J.M.D. Perspective and prospects for rare earth permanent magnets. *Engineering* **2020**, *6*, 119–131. [CrossRef]
3. München, D.D.; Stein, R.T.; Veit, H.M. Rare earth elements recycling potential estimate based on end-of-life ndfeb permanent magnets from mobile phones and hard disk drives in brazil. *Minerals* **2021**, *11*, 1190. [CrossRef]
4. Li, W.; Yang, L.J.; Zhang, Q.K.; Xu, C.; Zhu, Q.H.; Song, Z.L.; Zheng, B.Z.; Hu, F.Q.; Jiang, J.J. Effect of the grain boundary tb/dy diffused microstructure on the magnetic properties of sintered nd-fe-b magnets. *J. Magn. Magn. Mater.* **2020**, *502*, 7. [CrossRef]
5. Hioki, K. Development of high-performance hot-deformed neodymium–iron–boron magnets without heavy rare-earth elements. *Materials* **2023**, *16*, 6581. [CrossRef] [PubMed]
6. Schäfer, L.; Skokov, K.; Maccari, F.; Radulov, I.; Koch, D.; Mazilkin, A.; Adabifiroozjaei, E.; Molina-Luna, L.; Gutfleisch, O. A novel magnetic hardening mechanism for nd-fe-b permanent magnets based on solid-state phase transformation. *Adv. Funct. Mater.* **2023**, *33*, 2208821. [CrossRef]

7. Shuai, Z.C.; Zhu, Y.M.; Gao, P.; Han, Y.X. Rare earth elements resources and beneficiation: A review. *Miner. Eng.* **2024**, *218*, 17. [CrossRef]
8. Yang, W.Y.; Wu, K.J.; Chen, H.; Huang, J.; Yu, Z. Emerging role of rare earth elements in biomolecular functions. *Isme J.* **2025**, *19*, 16. [CrossRef]
9. Koese, M.; Parzer, M.; Sprecher, B.; Kleijn, R. Self-sufficiency of the european union in critical raw materials for e-mobility. *Resour. Conserv. Recycl.* **2025**, *212*, 10. [CrossRef]
10. Niskanen, J.; Lahtinen, M.; Perämäki, S. Acetic acid leaching of neodymium magnets and iron separation by simple oxidative precipitation. *Cleaner Eng. Technol.* **2022**, *10*, 9. [CrossRef]
11. Jones, K.G.; David, T.; Loula, M.; Matejková, S.; Blahut, J.; Filimonenko, A.; Litecká, M.; Rohlícek, J.; Böserle, J.; Polasek, M. Macrocyclic chelators for aqueous lanthanide separations via precipitation: Toward sustainable recycling of rare-earths from ndfeb magnets. *J. Am. Chem. Soc.* **2025**, *147*, 22666–22676. [CrossRef] [PubMed]
12. Dudarko, O.; Kobylinska, N.; Kessler, V.; Seisenbaeva, G. Recovery of rare earth elements from ndfeb magnet by mono- and bifunctional mesoporous silica: Waste recycling strategies and perspectives. *Hydrometallurgy* **2022**, *210*, 14. [CrossRef]
13. Jung, Y.; Lee, Y.; Yoon, S.J.; Choi, J.W. Synergistic effect of core/shell-structured composite fibers: Efficient recovery of rare-earth elements from spent ndfeb permanent magnets. *Adv. Fiber Mater.* **2024**, *6*, 1729–1745. [CrossRef]
14. Gergoric, M.; Ravaux, C.; Steenari, B.M.; Espegren, F.; Retegan, T. Leaching and recovery of rare-earth elements from neodymium magnet waste using organic acids. *Metals* **2018**, *8*, 721. [CrossRef]
15. Gergoric, M.; Ekberg, C.; Foreman, M.R.S.; Steenari, B.M.; Retegan, T. Characterization and leaching of neodymium magnet waste and solvent extraction of the rare-earth elements using todga. *J. Sust. Metall.* **2017**, *3*, 638–645. [CrossRef]
16. Liu, J.; Zhao, Y.X.; Wang, Z.R.; Jia, M.H.; Xia, W.X.; Wu, G.Z.; Guo, W.D.; Chi, R.A.; Huang, K. Review on micro-mechanism of forming emulsification during rare earth extraction by acidic extractants. *J. Rare Earths* **2025**, *43*, 9–20. [CrossRef]
17. Zeng, B.; Zeng, X.R.; Huang, L.J.H.; Huang, W.F.; Shu, R.H. Adsorption properties of a polyamine special ion exchange resin for removing molybdenum from ammonium tungstate solutions. *Sustainability* **2023**, *15*, 3837. [CrossRef]
18. Nogueira, M.; Matos, I.; Bernardo, M.; Pinto, F.; Fonseca, I.; Lapa, N. Recovery of nd^{3+} and dy^{3+} from e-waste using adsorbents from spent tyre rubbers: Batch and column dynamic assays. *Molecules* **2025**, *30*, 92. [CrossRef]
19. Zhong, Y.L.; Ning, S.Y.; Wu, K.; Li, Z.Y.; Wang, X.P.; He, C.L.; Fujita, T.; Wang, J.; Chen, L.F.; Yin, X.B.; et al. Novel phosphate functionalized sodium alginate hydrogel for efficient adsorption and separation of nd and dy from co. *J. Environ. Manag.* **2024**, *353*, 12. [CrossRef]
20. Jasim, A.Q.; Ajjam, S.K. Removal of heavy metal ions from wastewater using ion exchange resin in a batch process with kinetic isotherm. *S. Afr. J. Chem. Eng.* **2024**, *49*, 43–54. [CrossRef]
21. Yan, X.F.; Zhen, H.G.; Wang, B.; Yang, L. Selectivity and competitive mechanism of cation exchange resin for fe, mg, and al ions in phosphoric acid. *Can. J. Chem. Eng.* **2024**, *102*, 1272–1288. [CrossRef]
22. El-Din, A.S.M.; Rizk, H.E.; Borai, E.H.; El Afifi, E.M. Selective separation and purification of cerium (iii) from concentrate liquor associated with monazite processing by cationic exchange resin as adsorbent. *Chem. Pap.* **2023**, *77*, 2525–2538. [CrossRef]
23. Hong, H.J.; Yoo, H.; Jeon, J.H.; Kim, H.S.; Lee, J.Y. Differential adsorption of vanadium(v) and tungsten(w) on ion exchange resins: A novel approach for separation and recovery of spent catalyst leachate. *J. Clean. Prod.* **2023**, *426*, 11. [CrossRef]
24. Jiang, X.Z.; Luo, Y.H.; Mu, S.; Meng, B.J.; Wang, W.; Yu, G.; Deng, S.B. Structure-selectivity relationship of anion exchange resins with different quaternary amine functional groups for highly selective removal of pfas from chromium-plating wastewater. *Water Res.* **2025**, *268*, 10. [CrossRef] [PubMed]
25. Zhang, J.W.; Wu, W.L.; Gao, Y.C.; Zhao, S.H.; Zong, Y.M.; Xue, G.; Song, Y.H.; Ding, L. Efficient removal of nitrophenol by magnetic ion exchange resins: Role of nitrophenol functional groups based on characterisation, dft calculations and site energy distributions. *Sep. Purif. Technol.* **2025**, *354*, 15. [CrossRef]
26. Kovalenko, O.V.; Baulin, V.E.; Shulga, Y.M.; Baulin, D.; Tsivadze, A.Y. Recovery and separation of pr, nd, and dy using solvent impregnated resin from e-wastes. *J. Chromatogr. A* **2026**, *1765*, 10. [CrossRef]
27. Hermassi, M.; Granados, M.; Valderrama, C.; Skoglund, N.; Ayora, C.; Cortina, J.L. Impact of functional group types in ion exchange resins on rare earth element recovery from treated acid mine waters. *J. Clean. Prod.* **2022**, *379*, 13. [CrossRef]
28. Cui, Y.; Gao, S.; Zhang, R.; Cheng, L.; Yu, J. Study on the moisture absorption and thermal properties of hygroscopic exothermic fibers and related interactions with water molecules. *Polymers* **2020**, *12*, 98. [CrossRef]
29. Wang, X.Z.; Zheng, Y.H.; Xue, Y.; Yan, Y.D.; Ma, F.Q.; Zhang, M.L.; Bai, H.Y.; Kou, Z.Q.; Liu, J.P. Study on the destruction process of cationic exchange resins treated by Li_2CO_3-Na_2CO_3-K_2CO_3 molten salt. *J. Environ. Chem. Eng.* **2021**, *9*, 10. [CrossRef]
30. Jankovic, B.; Dodevski, V.; Veljkovic, F.; Jankovic, M.; Manic, N. Application of model-free and model-based kinetic methods in evaluation of reactions complexity during thermo-oxidative degradation process: Case study of 4-(hydroxymethyl)phenoxymethyl polystyrene resin. *Fire* **2024**, *7*, 165. [CrossRef]

31. Shah, K.H.; Shah, N.S.; Khan, G.A.; Sarfraz, S.; Iqbal, J.; Batool, A.; Jwuiyad, A.; Shahida, S.; Han, C.; Wawrzkiewicz, M. The cr(iii) exchange mechanism of macroporous resins: The effect of functionality and chemical matrix, and the statistical verification of ion exchange data. *Water* **2023**, *15*, 3655. [CrossRef]
32. Shimizu, S.; Matubayasi, N. Sorption hysteresis: A statistical thermodynamic fluctuation theory. *Langmuir* **2024**, *40*, 11504–11515. [CrossRef] [PubMed]
33. Otter, D.; Mondal, S.S.; Alrefai, A.; Krätz, L.; Holdt, H.J.; Bart, H.J. Characterization of an isostructural mof series of imidazolate frameworks potsdam by means of sorption experiments with water vapor. *Nanomaterials* **2021**, *11*, 1400. [CrossRef] [PubMed]
34. Babazadeh, M.; Irannezhad, M.; Abolghasemi, H.; Hosseiniyan, S.B.; Ehsani, A. 3d mathematical modeling of external mass transfer effect in high-rate adsorption process. *Surf. Interfaces* **2022**, *29*, 11. [CrossRef]
35. Chiu, H.-H.; Ho, M.-K.; Hsu, T.-E.; Yu, S.-L.; Manjunatha, K.; Cheng, C.-L.; Li, T.-Y.; Chang, C.-K.; Tummala, S.; Ho, Y.-P.; et al. Manipulating and investigating the room-temperature magnetic memory phenomenon: The impact of rare-earth ion doping on nickel oxide nanoparticles. *Mater. Today Chem.* **2024**, *39*, 102190. [CrossRef]
36. Chen, X.; Wang, C.; Li, M.; Zhang, D.; Wei, Y. Preparation of polydentate phosphonate-functionalized adsorbent for selective extraction of rare earth ions in harsh acidic solution. *Microchim. Acta* **2025**, *192*, 304. [CrossRef]
37. Vareda, J.P. On validity, physical meaning, mechanism insights and regression of adsorption kinetic models. *J. Mol. Liq.* **2023**, *376*, 14. [CrossRef]
38. Ho, Y.S.; McKay, G. Pseudo-second order model for sorption processes. *Process Biochem.* **1999**, *34*, 451–465. [CrossRef]
39. Wang, J.L.; Guo, X. Rethinking of the intraparticle diffusion adsorption kinetics model: Interpretation, solving methods and applications. *Chemosphere* **2022**, *309*, 14. [CrossRef]
40. Wei, F.; Jin, S.L.; Yao, C.Y.; Wang, T.H.; Zhu, S.P.; Ma, Y.B.; Qiao, H.; Shan, L.X.; Wang, R.C.; Lian, X.X.; et al. Revealing the combined effect of active sites and intra-particle diffusion on adsorption mechanism of methylene blue on activated red-pulp pomelo peel biochar. *Molecules* **2023**, *28*, 4426. [CrossRef]
41. Mikolajczyk, A.P.; Fortela, D.L.B.; Berry, J.C.; Chirdon, W.M.; Hernandez, R.A.; Gang, D.D.; Zappi, M.E. Evaluating the suitability of linear and nonlinear regression approaches for the langmuir adsorption model as applied toward biomass-based adsorbents: Testing residuals and assessing model validity. *Langmuir* **2024**, *40*, 20428–20442. [CrossRef]
42. Debnath, S.; Das, R. Strong adsorption of cv dye by ni ferrite nanoparticles for waste water purification: Fits well the pseudo second order kinetic and freundlich isotherm model. *Ceram. Int.* **2023**, *49*, 16199–16215. [CrossRef]
43. Mudhoo, A. Unveiling new insights: Revised temkin adsorption isotherm parameters from fresh curve fits in adsorption studies. *Chem. Eng. Sci.* **2025**, *311*, 14. [CrossRef]
44. Hu, Q.L.; Zhang, Z.Y. Application of dubinin-radushkevich isotherm model at the solid/solution interface: A theoretical analysis. *J. Mol. Liq.* **2019**, *277*, 646–648. [CrossRef]
45. Zhou, J.; Zhang, X.Y.; Deng, B.C.; Huang, Y.B.; Liu, X.J.; Ning, S.Y.; Kuang, S.T.; Liao, W.P. Separation and purification of heavy rare earth elements by a silica/polymer-based β-aminophosphonic acid resin from chloride media. *Sep. Purif. Technol.* **2025**, *354*, 9. [CrossRef]
46. Salvestrini, S.; Bollinger, J.C. Revisiting the extended van't hoff equation: Comments on "highly-efficient nitrogen self-doped biochar for versatile dyes' removal prepared from soybean cake via a simple dual-templating approach and associated thermodynamics". *J. Clean Prod.* **2022**, *373*, 4. [CrossRef]
47. Li, B.; Deng, Z.Y.; Lin, X.Y.; Chen, W.T.; Li, P.; Wu, J.H. Improved pb(ii) removal by d001 resin with a facile nanoscale α-feooh modification. *J. Environ. Chem. Eng.* **2024**, *12*, 9. [CrossRef]
48. Tang, L.; Lu, Y.Y.; Yao, L.L.; Cui, P. A highly hydrophilic benzenesulfonic-grafted graphene oxide-based hybrid membrane for ethanol dehydration. *RSC Adv.* **2020**, *10*, 20358–20367. [CrossRef]
49. Dyussembayeva, G.; Jumadilov, T.; Grazulevicius, J.; Mukatayeva, Z.; Khimersen, K.; Totkhuskyzy, B. Selective gold ion sorption from iron-containing solution using an interpolymer system of industrial ion exchangers. *Polymers* **2025**, *17*, 2808. [CrossRef]
50. Bai, Y.; Meng, Y.Y.; Yang, M.; Tian, R.J.; Wang, J.N.; Jiao, B.X.; Pan, H.B.; Gao, J.W.; Wang, Y.H.; Sun, K.X.; et al. Lattice stabilization and strain homogenization in sn-pb bottom subcells enable stable all-perovskite tandems solar cells. *Nat. Commun.* **2025**, *16*, 15. [CrossRef]
51. Zhang, P.; Lo, I.; O'Connor, D.; Pehkonen, S.; Cheng, H.F.; Hou, D.Y. High efficiency removal of methylene blue using sds surface-modified $znfe_2o_4$ nanoparticles. *J. Colloid Interface Sci.* **2017**, *508*, 39–48. [CrossRef]
52. Eltaweil, A.S.; Abdelfatah, A.M.; Hosny, M.; Fawzy, M. Novel biogenic synthesis of a ag@biochar nanocomposite as an antimicrobial agent and photocatalyst for methylene blue degradation. *ACS Omega* **2022**, *7*, 8046–8059. [CrossRef]
53. Henning, L.M.; Simon, U.; Abdullayev, A.; Schmidt, B.; Pohl, C.; Guitar, T.N.; Vakifahmetoglu, C.; Meyer, V.; Bekheet, M.F.; Gurlo, A. Effect of fomes fomentarius cultivation conditions on its adsorption performance for anionic and cationic dyes. *ACS Omega* **2022**, *7*, 12. [CrossRef] [PubMed]

54. Guo, X.T.; Wang, W.Q.; Lin, L.T.; Shan, J.; Zhu, J.Y.; Ning, S.P.; Li, H.M.; Wang, X.W.; Lu, D.C. Mnga with multiple enzyme-like properties for acute wound healing by reducing oxidative stress and modulating signaling pathways. *Mater. Today Bio* **2025**, *30*, 11. [CrossRef] [PubMed]
55. Sentürk, M.; Inan, S. Sorption and separation studies of nd(iii) and dy(iii) using amorphous tin(iv) phosphate. *Chem. Pap.* **2023**, *77*, 3835–3845. [CrossRef]
56. Virtanen, E.J.; Kukkonen, E.; Yliharju, J.; Tuomisto, M.; Frimodig, J.; Kinnunen, K.; Lahtinen, E.; Hännien, M.M.; Väisänen, A.; Haukka, M.; et al. Recovery of rare earth elements from mining wastewater with aminomethylphosphonic acid functionalized 3d-printed filters. *Sep. Purif. Technol.* **2025**, *353*, 12. [CrossRef]

Disclaimer/Publisher's Note: The statements, opinions and data contained in all publications are solely those of the individual author(s) and contributor(s) and not of MDPI and/or the editor(s). MDPI and/or the editor(s) disclaim responsibility for any injury to people or property resulting from any ideas, methods, instructions or products referred to in the content.